Discover Nano

Research

Green synthesis of silica-coated gold nanoparticles employing femtosecond laser, solid targets, and water

N. G. P. Machado[1] · M. P. Raele[1] · E. Jimenez-Villar[2] · W. de Rossi[1]

Received: 24 May 2024 / Accepted: 4 November 2024

Abstract
Gold nanoparticles are widely used in biomedical applications due to their unique properties. However, traditional synthesis methods generate contaminants that cause cytotoxicity and compromise the biocompatibility of the nanomaterials. Therefore, green synthesis methods are essential to produce pure and biocompatible nanoparticles, ensuring their effectiveness in biomedical applications. This study introduces a novel approach for synthesizing silica-coated gold nanoparticles ($AuNP@SiO_2$) using femtosecond laser ablation in water, eliminating the need for chemical reagents. The process involves three key laser-based steps: Si ablation, $SiNP@SiO_2$ fragmentation, and Au ablation, all conducted in a liquid environment. The resulting $AuNP@SiO_2$ were characterized using transmission electron microscopy (TEM), UV–Vis absorption spectroscopy, dynamic light scattering (DLS), X-ray diffraction (XRD), and zeta potential measurements. The results demonstrated that the $AuNP@SiO_2$ nanoparticles exhibit high colloidal stability, with a notably negative zeta potential of (-72.0 ± 0.3) mV, effectively preventing particle aggregation. TEM analysis confirmed predominantly spherical nanoparticles with an average diameter of (15.87 ± 0.70) nm, encapsulated by a SiO_2 layer ranging from 1 to 3 nm in thickness. The synthesis approach produced nanoparticles with an average size distribution below 35 nm. This green synthesis method not only produces stable and well-characterized $AuNP@SiO_2$ nanoparticles but also represents a significant step towards more sustainable nanomaterial production, with promising implications for biomedical applications.

Keywords Femtosecond laser ablation · Gold nanoparticles · Silica coating · Sustainable synthesis · Green nanoparticles · Biomedical applications

1 Introduction

Metallic nanoparticles (NPs), due to their electronic and optical properties (localized surface plasmon resonance, LSPR, and surface-enhanced Raman scattering, SERS) [1], have shown several applications such as drug delivery [2], biosensing [3], photodynamic [4, 5], photothermal therapy [6], imaging [7, 8], food industry [9] and cancer therapy [10]. However, for their biological use, it is important to control mainly their toxicity and colloidal stability. To provide the latter requirements, NPs have to be protected or encapsulated with organic capping agents such as amines, thiols, and polymers or oxides such as TiO_2 and SiO_2. Silica is particularly advantageous for solubility, low density, and the inertness of NPs while introducing numerous possibilities for their use [11–13]

Therefore, a synthesis method which assures low cytotoxicity and colloidal stability is desired in applications where the NPs itself should not present harmfulness or side effects. The suspension should also not present harmful residual

---

✉ M. P. Raele, mpraele@ipen.br | [1]Nuclear and Energy Research Institute, IPEN, CNEN/SP, Av. Prof. Lineu Prestes, 2242, São Paulo, SP CEP05508-000, Brazil. [2]The College of Optics and Photonics, CREOL, University of Central Florida, Orlando, FL 32816, USA.

Discover Nano (2025) 20:17 | https://doi.org/10.1186/s11671-024-04141-2

chemical reagents. In this way, a green synthesis [14] route is desired. A capping that allows functionalization of the NPs also is important to broadening its application range.

Ways of producing it, for instance, are via chemical reduction [15], electrochemical [16], photochemical [17] among others. Laser-assisted ways of synthesis are also possible, particularly in targets immersed in liquid [8], where the ablation of a solid target can create NPs by the condensation of the plasma formed in the process [18].

Laser ablation is a process in which a high-intensity laser pulse promotes a rapid phase transition of a target, usually from solid to plasma. In order to achieve it, nanosecond or shorter-duration pulses are applied, with considerable differences between them [19] with regard to the physical processes involved. In general terms, nanosecond ablation is ruled by thermal heating, resulting in a composition of liquid and vapor phases, whereas femtosecond ablation involves much more complex physical phenomena, with important differences between dielectrics and metals [20]. Thus, obtaining efficient ionization and atomization of the target, desirable for the production of nanoparticles, requires an adequate balance between the various parameters involved in the ablation process when ultrashort laser pulses are used [21].

The ablation and formation of metallic NPs is a half-step in the process. Nude NPs are prone to agglomeration [22], impairing its uses. Typically, nanoparticles display size-dependent instability when dispersed in a solution, leading to their tendency to aggregate into larger particles and subsequently precipitate. To avoid this issue, it is essential to shield or encapsulate nanoparticles using organic capping agents, including thiols, amines, and polymers, or by employing oxides such as SiO_2 [12, 23].

Previous studies have achieved metallic and capped NPs (shell-core) via laser ablation of solid targets, however, in these demonstrations, chemical solutions were applied [1, 24–26], which can impair the potential application of its products.

The aim of this study is to achieve a stable suspension of gold nanoparticles coated with SiO_2, entirely avoiding the use of chemical reagents.

Although some studies have demonstrated success in producing Si/Au nanocomposites via laser ablation in a liquid medium [27–29], primarily by mixing a suspension of silicon nanoparticles (SiNPs) with a suspension of gold nanoparticles (AuNPs), the methodologies used and the characteristics of the obtained nanomaterials show significant differences compared to the present study, which focuses on the synthesis of core–shell type nanoparticles.

Our proposal involves ablating a gold target immersed in water saturated with sub-nanometric SiO_2 particles (SiO_2NPs). During the ablation process, the ejected gold atoms coalesce to form AuNPs. These AuNPs will attract the dispersed SiO_2NPs due to their electrical affinity, resulting in the capping and stabilization of the gold nanoparticles. The resulting SiO_2-coated nanoparticles will be referred to as AuNP@SiO_2.

To create saturated water with SiO_2NPs, an immersed target of silicon can also be laser ablated, creating SiNPs whose surface is oxidated to form core–shell SiNP@SiO_2 [30], which is not ideal for our purpose due to its large size. However, it has been demonstrated that ns laser pulses can fragment these NPs in smaller pieces [31] enabling, in this way, adequate encapsulation of gold NPs.

This procedure leads to a three-step process (see Fig. 1): A) Silicon ablation in water; B) Fragmentation of the SiNP@SiO_2 and C) Ablation of the gold target immersed in the previously produced solution.

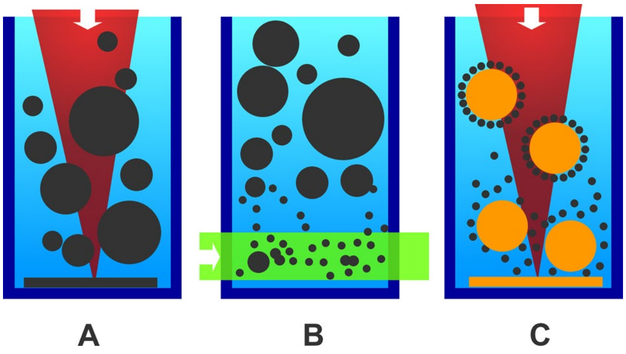

Fig. 1 Steps **A** ablation of a Si target, **B** fragmentation and oxidation of the SiNP@SiO_2 (large) leading to small SiO_2NPs, and **C** gold target ablation in SiO_2NPs suspension leading to the formation of AuNPs coated with silica shell (AuNP@SiO_2). Arrows indicate the laser incidence. (Illustration is not meant to represent the scales)

2 Materials and methods

For the production of green nanoparticles (AuNP@SiO_2), two different laser systems were employed. The primary femtosecond system was utilized for ablating solid targets, while the secondary nanosecond system was employed to induce SiNPs fragmentation and its subsequent total oxidation (silica).

The femtosecond laser pulses used were produced by the "Element PRO 400" seeder, whose emission is amplified by the "Femtopower Double 10 kHz" amplifier, both manufactured by Femtolasers Produktions GmbH. The system delivers 30 fs pulses centered at 800 nm with a bandwidth of 40 nm, in a pulse train with a 10 kHz repetition rate and maximum energy per pulse of 200 µJ. A high-precision micromachining stage (Aerotech, model ANT130) was utilized in combination with the mentioned laser system. The laser beam was focused onto the target surfaces using a 20-mm focal length lens.

For the scanning speed utilized of 4.5 mm/s and a repetition rate of 10 kHz, an overlap of 8 pulses was employed to ablate the targets. Furthermore, without considering the presence of liquid, the calculated diameter of the laser beam at the focal point on the target surface is 3.6 µm, which results in a fluence of 180 J/cm^2 for the energy used of 18 µJ. These values, however, are approximations because, in addition to the spherical aberration introduced by refraction at the water surface [32, 33], the calculated intensity of 5.9×10^{15} W/cm^2 at the focus is sufficient for the emergence of non-linear phenomena such as beam self-focusing [34], which modifies the entire spatial distribution of the focused laser pulse.

The secondary system utilized was a nanosecond laser (Nd:YAG) model "Merion—C" from Lumibird. It has a temporal width of 7 ns, with a maximum energy of 100 mJ, a repetition rate of 100 Hz, using a second harmonic generator and maximized for 532 nm, and a beam diameter of 5.5 mm without the use of focusing optics. The collimated beam was employed for Si fragmentation and subsequent production of SiO_2 NPs suspension.

The only materials utilized in nanoparticle production were ultrapure water, a gold target measuring 6 × 6x1 mm, and a pure single-crystal silicon target measuring approximately 5 × 5x1 mm. The irradiation protocol adhered to the following procedure:

1) Ablation of the Si target using the femtosecond laser: The silicon wafer was placed inside a cuvette, followed by the addition of ultrapure water (18.2 MΩ·cm) until it reached a height of 7 mm above the target surface. The Si surface was then ablated with ultrashort 30 fs pulses, with an energy of 42 µJ and a fluence of 180 J/cm^2 at the focal point. The ablation was conducted for 6 min, scanning the target surface at a speed of 4.5 mm/s. After the ablation, the initial solution exhibited a light brown color, indicating the presence of large SiNP@SiO_2 particles, which were unsuitable for the encapsulation of AuNPs.

2) SiNP@SiO_2 fragmentation using the nanosecond laser: To fragment the SiNP@SiO_2, the initial suspension was irradiated with a nanosecond laser, promoting the fragmentation of these nanoparticles and the oxidation of silicon, resulting in the formation of subnanometric SiO_2NPs. For this procedure, a cuvette (10 × 10x8 mm) containing the initial solution was positioned 40 cm away from the nanosecond laser and irradiated for 5 min with a pulse energy of 50 mJ, fluence of 210 mJ/cm^2, and a repetition rate of 100 Hz, no focusing lens was used. The laser beam was directed at the central lower area of the cuvette, ensuring uniform irradiation of the entire liquid volume through convection generated by the laser's interaction with the suspension, as illustrated in step 3 of Fig. 1.

3) Production of AuNP@SiO_2 using the femtosecond laser: The gold target was placed in the same cuvette used to irradiate the silicon target, followed by the addition of the SiO_2NPs solution produced in the previous step, filling the cuvette to a height of 7 mm above the Au surface. Subsequently, the gold target was ablated with the same parameters used in silicon ablation. Upon completion of the ablation process, the solution (AuNP@SiO_2) displayed a red hue, as shown in Fig. 2.

The AuNP@SiO_2 suspension was characterized using different techniques. The absorption spectrum was determined using UV–Vis spectroscopy, employing an Agilent "Cary 5000" spectrometer for this purpose. The hydrodynamic diameter and Zeta potential were assessed through dynamic light scattering (DLS) and electrophoretic light scattering (cmPALS) techniques, respectively, utilizing a particle analyzer model "Litesizer 500" from Anton Paar. Transmission electron microscopy (TEM) was employed to analyze the morphology and size distribution of the AuNP@SiO_2, utilizing a Jeol "JEM-2100" instrument. Additionally, X-ray diffraction (XRD) was utilized to examine the crystalline configuration of AuNP@SiO_2 and calculate the size of the crystallites, with Rigaku's "SmartLab" equipment being employed for this purpose.

To evaluate the productivity of AuNPs by measuring the mass quantity of Au in the synthesized nanoparticles, inductively coupled plasma mass spectrometry (ICP-MS) was employed. The analysis was conducted using the NexION

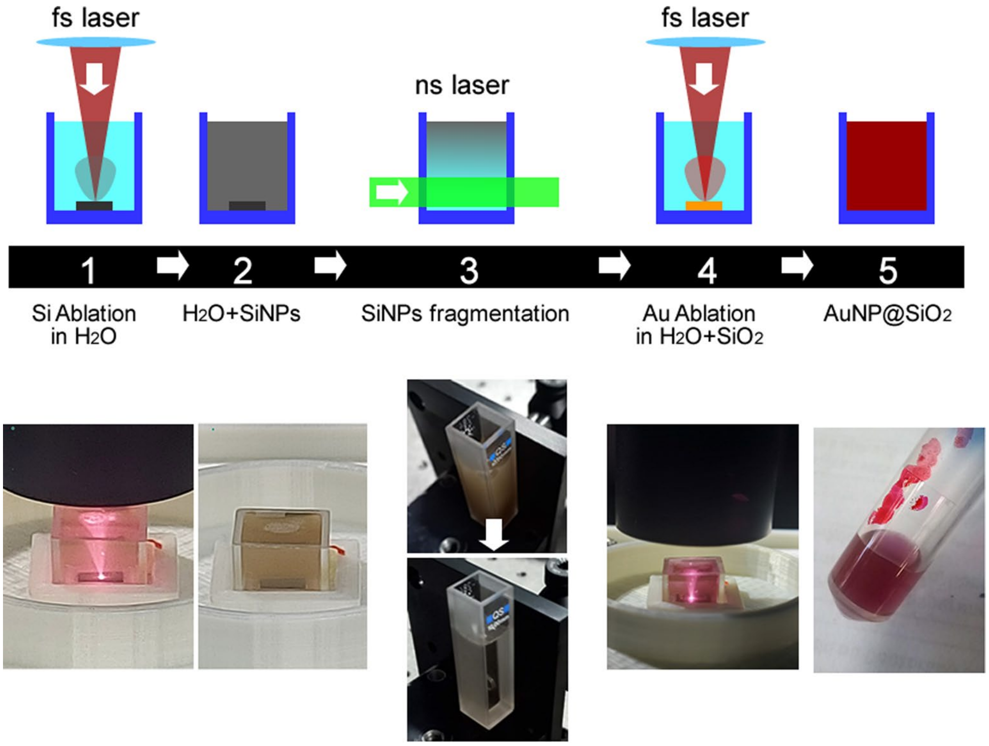

Fig. 2 At the top is shown a schematic illustration of the methodology: **1** The solid silicon target is ablated while immersed in ultrapure water; **2** The resulting solution undergoes irradiation to fragment the SiNPs superficially oxidated and their subsequent total oxidation, rendering a SiO_2NPs suspension completely clear; **4** The gold target immersed in SiO_2NPs suspension is ablated, leading to the formation of core–shell AuNP@SiO_2 as presented in step 5. At the bottom are shown the experimental results corresponding to the same steps

300D from Perkin Elmer. The AuNP solution was prepared in mass concentrations within the ng mL^{-1} range. For the size calibration curve of the sp-ICP-MS results, 30, 50, and 100 nm PEG-COOH gold nanosphere standards (NanoComposix) were used. A Spex plasma standard was used for dissolved gold calibration. The dwell time was 50 µs, the scan time was 100 s, the sample flow rate, measured gravimetrically, was 0.342 mL min^{-1}, and the transport efficiency was 6.42.

To conduct a crystallographic analysis of synthesized AuNPs@SiO_2, 8 ml of the suspension was accurately dispensed onto the surface of a GaAs < 100 > substrate. This substrate was selected due to its high purity and well-defined diffraction peaks, which aid in identifying the nanoparticles' diffraction pattern. The GaAs substrate was heated to 100 ºC, facilitating water evaporation and the formation of AuNPs@SiO_2 layer on the GaAs surface.

3 Results and discussion

3.1 SiO_2NPs suspension

As depicted in Fig. 1, the first step consisted of the Si target ablation (Fig. 2, step 1). The resulting suspension (at the bottom of Fig. 2, step 2) presented a brownish turbid appearance. Its absorbance spectrum presented specific features, such as resonance bands at the visible window (Fig. 3).

The suspension was fragmented using the referred laser and methodology for 5 min, however, the solution became completely transparent approximately 2 min after the irradiation started. Figure 3 also presents its absorbance spectrum.

The absorbance presented in Fig. 3 for the initial solution exhibits the characteristic pattern of silicon nanoparticles (SiNPs) [35]. On the other hand, the fragmented solution demonstrates the typical pattern of a silica solution [36]. It is noteworthy that the absorbance of the fragmented solution at the femtosecond laser wavelength is nearly zero, indicating minimal linear energy loss of the beam as it traverses the liquid medium during the Au ablation process, with the energy loss being only 0.04% for the optical path used.

The difference in absorbance between the two solutions is mainly due to the sequence of chemical phenomena caused by the SiNP@SiO_2 fragmentation in the initial solution. Irradiation of the solution with the nanosecond laser provides energy to the Si structure, causing electronic excitation. During the de-excitation process, the electrons transfer thermal energy to the crystalline network of the nanoparticle, resulting in an increase in the temperature of

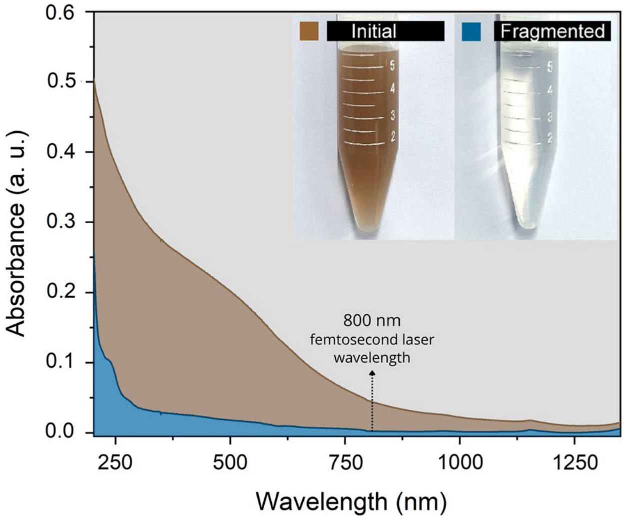

Fig. 3 Absorbance spectrum of the initial SiNP@SiO_2 suspension after fs laser ablation (brown) and after the fragmentation by the ns laser pulse irradiation (blue). The visual aspect of the two solutions is presented in the photographs at right side

the SiNPs. This temperature increase, in turn, leads to breaking bonds between the Si atoms, causing the fragmentation of the nanoparticles.

Due to the SiNPs fragmentation by their strong absorption at the wavelength of the nanosecond laser, smaller SiNPs are again superficially oxidized. This cycle is repeated several times until SiNPs reach a size small enough to be completely oxidized. Silicon oxidation occurs through the reaction $Si + 2H_2O \rightarrow SiO_2 + 2H_2$, releasing H_2 gas.

TEM analysis of dried samples from both the initial and fragmented suspensions, as shown in Fig. 4, revealed the presence of large SiNP clusters (> 2 µm) in the pre-irradiation sample (initial), which explains the turbid appearance of the suspension. Following laser irradiation, TEM images confirmed the efficient fragmentation of these clusters, driven by the oxidation of SiNPs into subnanometric SiO_2 particles. This process resulted in a clear, translucent solution, as depicted in Fig. 3.

The results found at Fig. 4 right are in accordance with Rioux et al. [27]. The Si oxidation process into SiO_2 has proven to be highly efficient, despite it is still possible to observe some Si nanoparticles in the TEM image shown in Fig. 4 (diameter ~ 7 nm).

It is worth noting that the absorbance of the fragmented SiO_2NPs suspension at the wavelength of the femtosecond laser is practically zero. This prevents absorption of the laser pulses away from the focal position, where multiphoton absorption takes place.

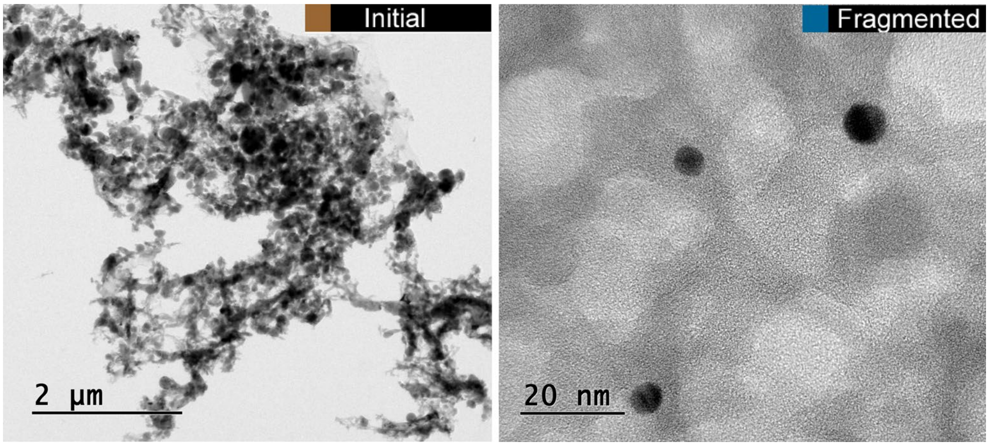

Fig. 4 TEM images of the ablated Silicon suspensions before (SiNP@SiO_2) and after laser fragmentation (SiO_2 suspension)

Fig. 5 UV–Vis spectrum of AuNP@SiO_2 produced with an ablation time of 6 min. The colloidal solutions had absorption peak centered at 522.05 nm

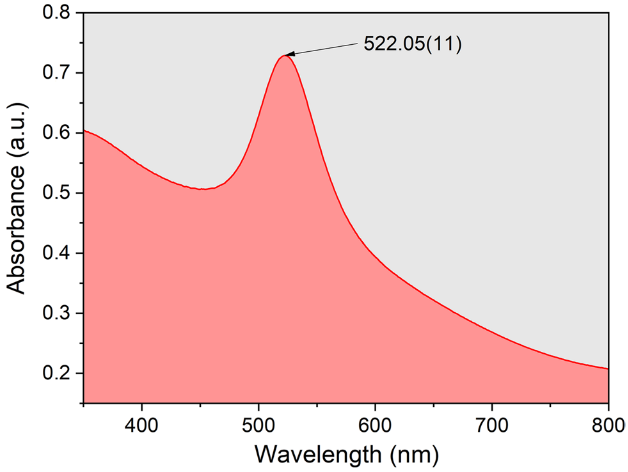

3.2 AuNP@SiO_2 Absorbance, DLS, and Zeta Potential

After the production of AuNPs@SiO_2 using the fragmented suspension, the absorbance of the nanoparticles was analyzed, as depicted in Fig. 5. The peak of Localized Surface Plasmon Resonance (LSPR) obtained was compared with nanoparticle size values reported in the literature.

The SPR peak at around 522 nm indicates an average diameter between 15–20 nm for monodisperse nanoparticles [37]. Although AuNPs@SiO_2 produced with femtosecond laser are polydisperse, this measurement provides an initial reference point for estimating the average diameter of the nanoparticles.

Other techniques, such as TEM and DLS, were employed to determine the diameter of nanoparticles. Therefore, this initial diameter estimation is refined based on information obtained from other measurements, which contribute to a more comprehensive understanding of the characteristics and the physical process involved in the production of these nanomaterials.

Nanoparticles are often characterized by the diameter of their cores; however, it has been often not given due attention to understand their physical behavior in colloidal solution. When comparing core diameter data with hydrodynamic diameter, two outcomes can be observed: the hydrodynamic diameter may be approximately equal to the core diameter, or significantly larger. This disparity between the two radii can vary considerably and is influenced by various factors such as nanoparticle size and shape, solvent properties, as well as the presence of adsorbed molecules or solvation layers.

A critical effect impacting the results presented in Fig. 6 is the presence of a significant solvation layer around the nanoparticles. Generally, this layer can have considerable thickness in situations where interactions between the

Fig. 6 Bimodal hydrodynamic diameter distribution for AuNP@SiO_2. The colloidal suspension has a main and a secondary population, respectively composed of approximately 91% and 9% of the total volume of nanoparticles

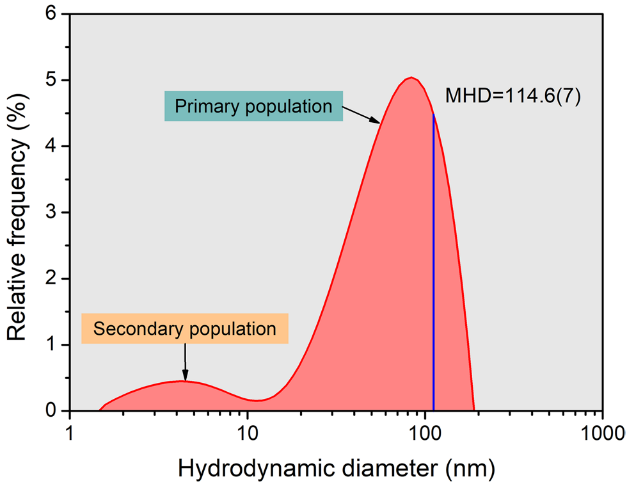

particle surface and the solvent are particularly intense. As a result, the hydrodynamic diameter, which accounts for this solvation layer, can be larger than the core diameter of the particle.

When comparing the mean hydrodynamic diameter (MHD), obtained through DLS technique, with the average size of nanoparticles obtained through absorbance, we can observe the existence of a significant solvation layer around the nanoparticles, with a thickness of approximately 47 nm.

The colloidal solution comprises two nanoparticle populations: a primary one, constituting approximately 91% of the total population, and a secondary one, representing around 9% of the total, composed of nanoparticles with hydrodynamic diameters smaller than 11 nm.

The presence of a secondary population of nanoparticles smaller than the primary population suggests that such population is originated by physical processes resulting in the fragmentation of the primary population.

It is worth noting here that the fragmentation processes of the target, or of the already formed NPs, are not fully established in the literature, as in addition to the direct ablation of the target by the laser pulse, the process of interaction of this ultrashort pulse with water causes the optical breakdown of the surrounding medium, with the development of various phenomena such as plasma formation, the production of very intense shock waves, cavitation and dissociation of water, with the formation of bubbles, among others. Therefore, the participation of each of these processes in the fragmentation of the solid medium is very difficult to establish.

Among the primary physical processes in nanoparticle fragmentation, the fluence of the laser and the re-irradiation of nanoparticles by subsequent pulses stand out. Higher fluence can result in more intense fragmentation of the primary nanoparticle population. Additionally, increasing the number of pulses incident on the same region intensifies this phenomenon, leading to the enhanced formation of the secondary nanoparticle population.

The zeta potential, being a measure of the surface charge of nanoparticles dispersed in the liquid, is crucial for understanding and controlling the stability of nanoparticles in suspension. Figure 7 presents the zeta potential value of the produced AuNP@SiO_2.

The obtained zeta potential of (-72.0 ± 0.3) mV suggests a highly stable solution due to the strong electrostatic repulsion between particles. This high negative zeta potential value indicates that the surface of the nanoparticles presents a strong electric field, resulting in effective dispersion and prevention of particle aggregation.

The concentration of AuNPs was quantified via ICP-MS, revealing a conversion of (11.2 ± 0.6) µg/mL of Au into nanoparticles after 6 min of ablation, corresponding to a productivity rate of 78.4 µg/h. This result highlights the efficiency of the synthesis process, demonstrating that the ablation time used consistently produces nanoparticles. Additionally, it is noted that increases in AuNP concentration can be achieved by adjusting parameters such as ablation time, laser energy, or repetition rate. These variables offer a wide range for process modulation, facilitating the customization of synthesis according to specific application requirements.

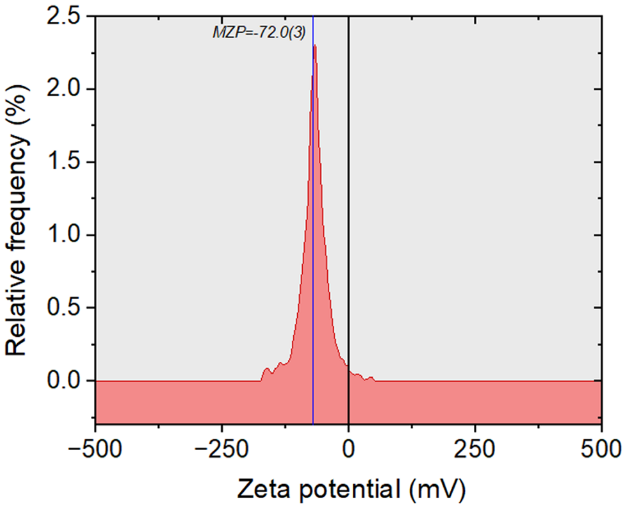

Fig. 7 Zeta potential distribution for AuNP@SiO_2 produced with an ablation time of 6 min. The mean zeta potential (-72.0 ± 0.3) mV explains the excellent colloidal stability

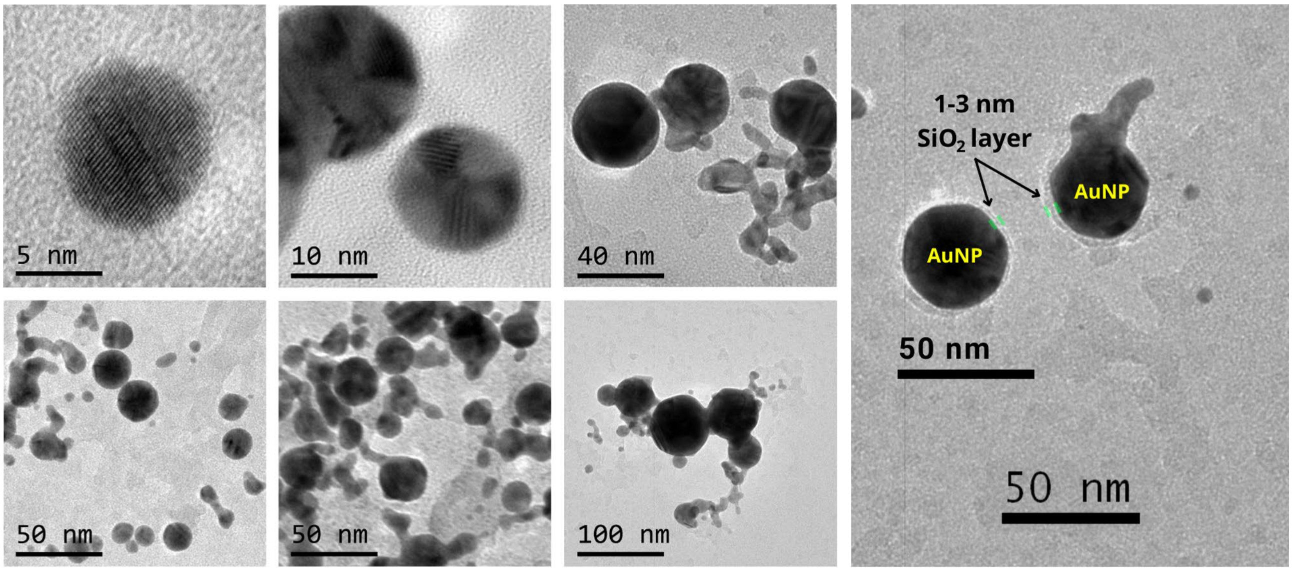

Fig. 8 TEM images of AuNP@SiO_2 synthesized with the femtosecond laser

3.3 AuNP@SiO_2 TEM and XRD

TEM measurements were performed to characterize the sizes and morphology of the AuNP@SiO_2 produced using the femtosecond laser. The transmission electron microscopy images presented in Fig. 8 reveal that the nanoparticles exhibit predominantly spherical shapes, with sizes smaller than 35 nm. Furthermore, it is observed that the SiO_2 layer formed on the surface of the nanoparticles has a thickness ranging from 1 to 3 nm.

Through TEM analysis, it was observed that the nanoparticles are below 35 nm in size, with an average size of (15.23 ± 0.92) nm, as shown in the histogram generated from the TEM data (Fig. 9). This average size aligns perfectly with the LSPR peak observed via UV–Vis measurement, Fig. 5.

Figure 9 presents the histogram resulting from the analysis of core sizes via TEM. Notably, two distinct peaks emerge in the distribution, each fitted to a Gaussian curve. The first peak, with an average size of (22.09 ± 0.89) nm, represents the primary population generated through femtosecond laser-induced ablation. Conversely, the second peak, averaging (10.41 ± 0.72) nm, is associated with laser-induced fragmentation [38]. This finding underscores a crucial phenomenon: nanoparticles originally formed via laser ablation of a solid in a liquid medium undergo subsequent fragmentation by laser pulses, resulting in a secondary population characterized by increased abundance and reduced size.

Fig. 9 Particle size distribution histogram of spherical Gold nanoparticles determined from TEM image. Solid line represents two distinct populations, with an average diameter of (15.23 ± 0.92) nm (dashed line)

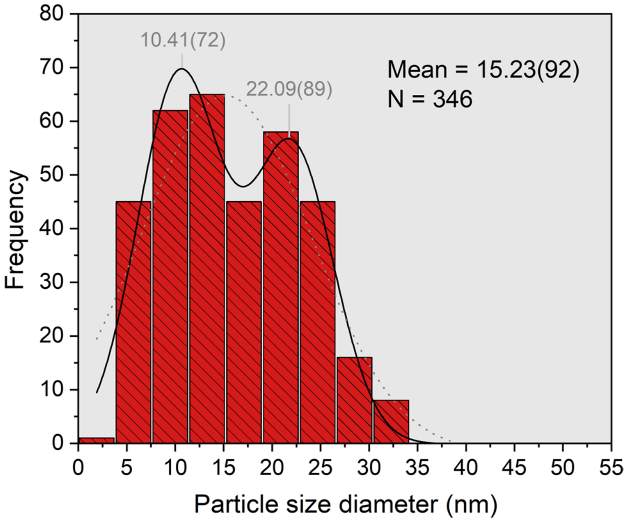

Fig. 10 Hydrodynamic diameter for AuNP@SiO2 produced with Au target irradiation time of 2 and 6 min. The mean hydrodynamic diameter of the gold nanoparticles produced at 2 min was (133 ± 58) nm, while for 6 min, it decreased to (129 ± 51) nm

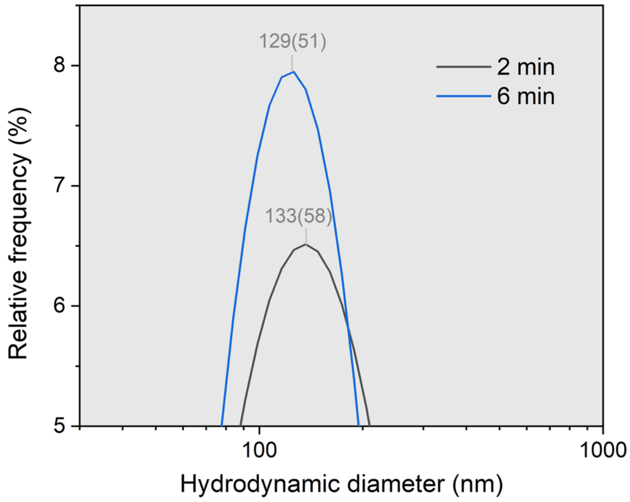

Fig. 11 XRD characterization of laser-produced green nanoparticles. The analysis enabled the identification of four crystalline Au phases, Si bulk residues, amorphous SiO_2, and GaAs substrate phases

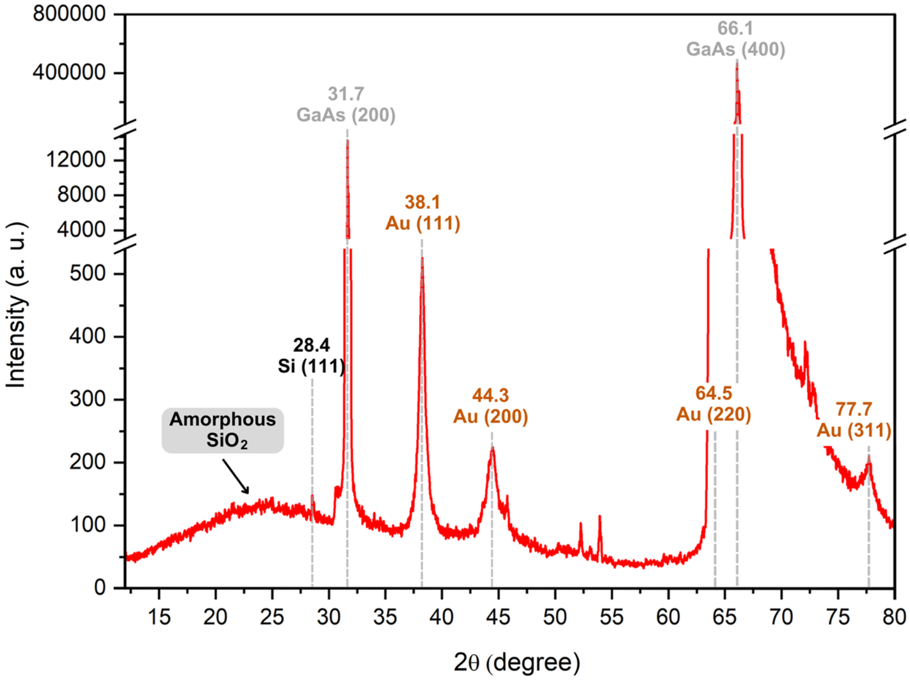

While the histogram of TEM measurements, presented in Fig. 9, exclusively reflects the core size of the gold nanoparticles, the DLS analysis, shown in Fig. 6, provides a broader view corresponding to the effective size of the nanoparticles in motion within the solution. The hydrodynamic diameter includes not only the core and the silica shell of the nanoparticle but also a layer of strongly adsorbed H_2O and SiO_2 molecules surrounding the particles (solvation layer). In the case of AuNP@SiO_2, this significant solvation layer, estimated at approximately 47 nm, results in a hydrodynamic diameter considerably larger than the physical core size observed in TEM measurements.

To investigate the occurrence of the fragmentation process of AuNP@SiO_2, responsible for the secondary population identified in Figs. 6 and 9, the NPs were synthesized by irradiating the gold target submerged in a suspension of SiO_2NPs for 2 min. The aim was to reduce the interaction time of the suspension with the laser, thereby decreasing the fragmentation process of the NPs. As a result, as demonstrated in Fig. 10, it was observed that the average hydrodynamic diameter after 2 min of irradiation is greater compared to 6 min, indicating that a longer interaction time of the suspension with the laser increases the fragmentation process, which, in turn, reduces the average hydrodynamic diameter of the AuNP@SiO_2.

The crystallinity of laser-synthesized AuNPs@SiO_2 was investigated by X-ray diffraction (XRD) technique, and corresponding XRD patterns were shown in Fig. 11. The two most intense peaks identified in the diffractogram correspond to gallium arsenide (GaAs), with 2θ angles of 31.7° and 66.1°. This substrate, characterized by its specific orientation and high purity (99.9%), was employed to facilitate the discernment of peaks associated with nanoparticles deposited on its surface.

Gold nanocrystals exhibited four distinctive peaks at 2θ angles of 38.1°, 44.3°, 64.5°, and 77.7°. These angles correspond to diffraction signal from the crystalline planes (111), (200), (220), and (311) of the face-centered cubic (fcc) lattice of gold, respectively. The intense diffraction at 38.1° peak shows that the preferred growth orientation of gold was fixed in (111) direction.

Using the Scherrer formula [39] it was possible to estimate the crystallite diameter of AuNPs@SiO_2 as calculated for different crystallographic diffraction directions: $D_{111} = (12.65 \pm 0.14)$ nm, $D_{200} = (7.26 \pm 0.17)$ nm, and $D_{311} = (11.13 \pm 0.24)$ nm. The average crystallite diameter was determined to be $D_{med} = (10.35 \pm 0.18)$ nm. The signal associated with the crystallographic direction Au_{220} was compromised due to the high intensity of the $GaAs_{400}$ signal originating from the substrate.

The XRD analysis also revealed the fragmentation process of the initial solution, aimed at converting the remaining Si_{111} from femtosecond laser ablation into SiO_2. This observation is supported by the fact that the peak associated with Si_{111} residues is minimal when compared to the curve of amorphous SiO_2.

4 Conclusion

This study presented an innovative and sustainable route for the synthesis of silica-coated gold nanoparticles (AuNP@SiO_2) using femtosecond laser ablation in a liquid medium. The simplicity and efficiency of the method are remarkable, employing only three materials—a silicon wafer, a gold target, and water—for the production of highly pure and stable nanoparticles, without the need for chemical reagents.

The technique enabled the rapid synthesis of nanoparticles in three steps, each lasting approximately 6 min. The resulting nanoparticles had predominantly sizes below 35 nm, with high colloidal stability confirmed by the highly negative zeta potential (-72.0 ± 0.3 mV), preventing particle aggregation. TEM analysis revealed spherical morphology with silica layers between 1 and 3 nm, while the diameter estimate from the LSPR peak (15–20 nm) aligns with the average value of (15.87 ± 0.70) nm observed in the size distribution. The core distribution also indicated sizes up to 32 nm.

These results demonstrate the efficacy of this green route for producing AuNP@SiO_2 free from harmful chemical residues, highlighting significant potential for biomedical and technological applications. Further optimization of the ablation parameters could enhance the uniformity and control of the process, allowing for broader application of these nanoparticles in biological applications.

Acknowledgements This study was financed, in part, by the São Paulo Research Foundation (FAPESP), process number 2013/26113-6. The authors acknowledge the support given by the Brazilian National Council for Scientific and Technological Development – CNPq, grants INFO 465763/2014-6, Sisfóton 440228/2021-2, and INCT 406761/2022-1 INTERAS. We also thank the Center for Lasers and Applications' Multiuser Facility at IPEN-CNEN/SP for the support given. We thank the Microscopy and Microanalysis Laboratory of CCTM-IPEN for using the TEM, and the Laboratory of Radioactive Sources for Radiotherapy at CETER-IPEN for using the DLS.

Author contribution Machado, N.G.P.: was responsible for planning and conducting the experiments, performing sample characterizations and data analysis, and writing the base text for the paper. de Rossi, W.: is an expert in femtosecond laser-matter interaction. He operated the laser during experiments, assisted in data analysis, and reviewed the manuscript. Raele: Contributed to the conceptualization of the experiment, data analysis, and manuscript review. Gimenes: Contributed to the conceptualization of the experiment, data analysis, and manuscript review.

Funding Brazilian National Council for Scientific and Technological Development – CNPq,INFO 465763/2014-6,INFO 465763/2014-6,INFO 465763/2014-6,INFO 465763/2014-6

Data availablity The data used in this study are available upon request. Interested parties can contact the main author via the email provided to obtain access to the data.

Declarations

Competing interests The authors declare no competing interests.

References

1. Nie SM, Emery SR. Probing single molecules and single nanoparticles by surface-enhanced Raman scattering. Science. 1997;275(5303):1102–6. https://doi.org/10.1126/science.275.5303.1102.
2. Tiwari PM, Vig K, Dennis VA, et al. Functionalized gold nanoparticles and their biomedical applications. Nanomaterials. 2011;1(1):31–63. https://doi.org/10.3390/nano1010031.
3. Homola J. Present and future of surface plasmon resonance biosensors. Anal Bioanal Chem. 2003;377(3):528–39. https://doi.org/10.1007/s00216-003-2101-0.
4. Fuertes G, Pedrueza E, Abderrafi K, et al. Photoswitchable bactericidal effects from novel silica-coated silver nanoparticles. Munich, GERMANY; 2011.
5. Fuertes G, Sánchez-Muñoz OL, Pedrueza E, et al. Switchable bactericidal effects from novel silica-coated silver nanoparticles mediated by light irradiation. Langmuir. 2011;27(6):2826–33. https://doi.org/10.1021/la1045282.
6. Huang XH, El-Sayed IH, Qian W, et al. Cancer cell imaging and photothermal therapy in the near-infrared region by using gold nanorods. J Am Chem Soc. 2006;128(6):2115–20. https://doi.org/10.1021/ja057254a.
7. Huang Y, Li M, Huang D, Qiu Q, Lin W, Liu J, Yang W, Yao Y, Yan G, Qu N, Tuchin VV. Depth-resolved enhanced spectral-domain OCT imaging of live mammalian embryos using gold nanoparticles as contrast agent. Small. 2019;15(35):1902346.
8. Felix E, Mánuel JM, Litrán R, et al. Scanning pulsed laser ablation in liquids: an alternative route to obtaining biocompatible YbFe nanoparticles as multiplatform contrast agents for combined MRI and CT imaging. Ceram Int. 2023;49(6):9324–37. https://doi.org/10.1016/j.ceramint.2022.11.099.
9. Hua Z, Yu T, Liu D, Xianyu Y. Recent advances in gold nanoparticles-based biosensors for food safety detection. Biosens Bioelectron. 2021;179:113076.
10. W. C, T. G, H. H, et al. Applications of gold nanoparticles in cancer nanotechnology. Nanotechnology, Science and Applications 2008, https://doi.org/10.2147/nsa.s3788
11. Jimenez-Villar E, Mestre V, de Oliveira PC, et al. Novel core-shell (TiO₂@Silica) nanoparticles for scattering medium in a random laser: higher efficiency, lower laser threshold and lower photodegradation. Nanoscale. 2013;5(24):12512–7. https://doi.org/10.1039/c3nr03603k.
12. Jiménez E, Abderrafi K, Abargues R, et al. Laser-ablation-Induced synthesis of SiO₂-capped noble metal nanoparticles in a single step. Langmuir. 2010;26(10):7458–63. https://doi.org/10.1021/la904179x.
13. Ermakov VA, Martins WS, Wetter NU, et al. Localization of light induced in ordered colloidal suspensions: powerful sensing tools. Nanoscale. 2021;13(13):6417–25. https://doi.org/10.1039/d0nr08736j.
14. Singh J, Dutta T, Kim KH, Rawat M, Samddar P, Kumar P. 'Green'synthesis of metals and their oxide nanoparticles: applications for environmental remediation. J nanobiotechnol. 2018;16:1–24.
15. De Souza CD, Nogueira BR, Rostelato ME. Review of the methodologies used in the synthesis gold nanoparticles by chemical reduction. J Alloys Compd. 2019;798:714–40.
16. Mahapatra SK, Bogle KA, Dhole SD, Bhoraskar VN. Synthesis of gold and silver nanoparticles by electron irradiation at 5–15 keV energy. Nanotechnology. 2007;18(13):135602.
17. McGilvray KL, Decan MR, Wang DS, et al. Facile photochemical synthesis of unprotected aqueous gold nanoparticles. J Am Chem Soc. 2006;128(50):15980–1. https://doi.org/10.1021/ja066522h.
18. Zeng HB, Du XW, Singh SC, et al. Nanomaterials via laser ablation/irradiation in liquid: a review. Adv Func Mater. 2012;22(7):1333–53. https://doi.org/10.1002/adfm.201102295.
19. Chichkov BN, Momma C, Nolte S, et al. Femtosecond, picosecond and nanosecond laser ablation of solids. Appl Phy Mater Sci Process. 1996;63(2):109–15. https://doi.org/10.1007/bf01567637.
20. Gamaly EG, Rode AV, Luther-Davies B, et al. Ablation of solids by femtosecond lasers: ablation mechanism and ablation thresholds for metals and dielectrics. Phys Plasmas. 2002;9(3):949–57. https://doi.org/10.1063/1.1447555.
21. Amendola V, Meneghetti M. Laser ablation synthesis in solution and size manipulation of noble metal nanoparticles. Phys Chem Chem Phys. 2009;11(20):3805–21. https://doi.org/10.1039/b900654k.
22. Pochapski DJ, dos Santos CC, Leite GW, et al. Zeta potential and colloidal stability predictions for inorganic nanoparticle dispersions: effects of experimental conditions and electrokinetic models on the interpretation of results. Langmuir. 2021;37(45):13379–89. https://doi.org/10.1021/acs.langmuir.1c02056.
23. González-Castillo JR, Rodriguez E, Jimenez-Villar E, Rodríguez D, Salomon-García I, de Sá GF, García-Fernández T, Almeida DB, Cesar CL, Johnes R, Ibarra JC. Synthesis of Ag@ Silica nanoparticles by assisted laser ablation. Nanoscale Res Lett. 2015;10:1–9.
24. Verma AK, Soni RK. Laser ablation synthesis of bimetallic gold-palladium core@ shell nanoparticles for trace detection of explosives. Opt Laser Technol. 2023;163:109429.
25. Jiménez E, Abderrafi K, Martínez-Pastor J, Abargues R, Valdés JL, Ibañez R. A novel method of nanocrystal fabrication based on laser ablation in liquid environment. Superlattices Microstruct. 2008;43(5–6):487–93.
26. John MG, Tibbetts KM. One-step femtosecond laser ablation synthesis of sub-3 nm gold nanoparticles stabilized by silica. Appl Surf Sci. 2019;475:1048–57. https://doi.org/10.1016/j.apsusc.2019.01.042.
27. Nasiri P, Doranian D, Sari AH. Synthesis of Au/Si nanocomposite using laser ablation method. Opt Laser Technol. 2019;113:217–24.

28. Al-Kattan A, Tselikov G, Popov AA, et al. Plasmonic Si@Au core-satellite nanoparticles prepared by laser-assisted synthesis for photothermal therapy. J Phys: Conf Ser. 2021;2058(1):012008. https://doi.org/10.1088/1742-6596/2058/1/012008.
29. Ryabchikov YV, Mirza I, Flimelová M, et al. Merging of Bi-modality of ultrafast laser processing: heating of Si/Au nanocomposite solutions with controlled chemical content. Nanomaterials. 2024;14(4):321. https://doi.org/10.3390/nano14040321.
30. Rioux D, Laferriere M, Douplik A, et al. Silicon nanoparticles produced by femtosecond laser ablation in water as novel contamination-free photosensitizers. Journal of Biomedical Optics 2009;14(2), https://doi.org/10.1117/1.3086608
31. Solati E, Dejam L, Dorranian D. Effect of laser pulse energy and wavelength on the structure, morphology and optical properties of ZnO nanoparticles. Opt Laser Technol. 2014;58:26–32.
32. Torok P, Varga P, Laczik Z, et al. Electromagnetic diffraction of light focused through a planar interface between materials of mismatched refractive-indexes - an integral-representation. J Opt Soc Am a-Opt Image Sci Vision. 1995;12(2):325–32. https://doi.org/10.1364/josaa.12.000325.
33. Gu M. Advanced Optical Imaging Theory. Berlin Heidelberg: Springer; 2013.
34. Gamaly EG. The physics of ultra-short laser interaction with solids at non-relativistic intensities. Phy Rep-Rev Sect Phy Lett. 2011;508(4–5):91–243. https://doi.org/10.1016/j.physrep.2011.07.002.
35. Zhao W, Ji W, Zhang YF, et al. A competitive fluorescence quenching-based immunoassay for bisphenol a employing functionalized silica nanoparticles and nanogold. RSC Adv. 2016;6(45):38950–6. https://doi.org/10.1039/c5ra26366b.
36. Zhang L, Wang X, Wei X. Evolution of grain structure and texture for 6082–T6 aluminum alloy during friction stir welding. J Wuhan Univ Technol-Mater Sci Ed. 2019;34(2):397–403.
37. Biswas NDBSBANR. Correlation of Surface Plasmon Resonance Wavelength (SPR) with Size and Concentration of Noble Metal Nanoparticles. Annals of reviews and research 2019, https://doi.org/10.19080/ARR.2019.04.555658
38. Bongiovanni G, Olshin PK, Yan CC, et al. The fragmentation mechanism of gold nanoparticles in water under femtosecond laser irradiation. Nanoscale Advances. 2021;3(18):5277–83. https://doi.org/10.1039/d1na00406a.
39. Valerio AaTFaPRaRBaDSaEMaRCaFAsaKSaMS. Proper usage of Scherrer's and Guinier's formulas in X-ray analysis of size distribution in systems of monocrystalline CeO2 nanoparticles. 2022;